SiC-Based Z-Source Resonant Converter With Constant Frequency and Load Regulation for EV Wireless Charger

Hulong Zeng, *Student Member, IEEE*, and Fang Z. Peng, *Fellow, IEEE*

***Abstract*—Traditional load regulation methods for a resonant converter mainly rely on frequency modulation. It is always a tradeoff between the design of the resonant network and the range of load. Especially for wireless power transfer (WPT) systems, the resonant network usually has a high quality factor. Small variation on frequency leads to huge drop in gain and efficiency. Due to this problem, many WPT systems are unregulated and they need one or two more front-end stages to regulate the dc bus voltage and perform power factor correction (PFC). In order to lower the cost and complexity of two- or three-stages structure, a single-stage solution with a silicon carbide (SiC) based Z-source resonant converter (ZSRC) was recently proposed. The Z-source network provides high reliability as being immune to shoot-through problems. Additionally, a ZSRC can boost the dc bus voltage while the traditional voltage-source inverter can only produce a lower voltage. However, the load regulation of this new topology has not been addressed. Two effective load regulation methods with constant frequency are presented for this SiC-based ZSRC specifically. Operation principle of the two load regulation methods are described in this paper. Experimental results based on a 200-W scale-down prototype with a full-bridge series resonant dc–dc converter are presented to illustrate the mechanism of these two methods.**

***Index Terms*—Electric vehicles (EVs), load regulation, resonant converter, silicon carbide (SiC), wireless power transfer (WPT), Z-source.**

I. Introduction

RESEARCH on wireless power transfer (WPT) for the electric vehicles (EVs) battery charger is actively carrying on, for the sake of its advantages of convenience, reliability, and environmental adaptation [1]. For a stationary application, a WPT charger system allows the driver simply to park and charge without getting out of the vehicle. Furthermore, a dynamic WPT charger system, also called online inductive power transfer (OLPT), can charge the running EVs with embedded transmit coils under a road (see Fig. 1). A proper energy storage and charging system design could reduce 20% battery capacity of the EVs [2], minimizing the weight and cost.

Manuscript received September 8, 2016; revised November 9, 2016; accepted December 11, 2016. Date of publication December 20, 2016; date of current version June 23, 2017. Recommended for publication by Associate Editor C. T. Rim.

The authors are with the Department of Electrical and Computer Engineering, Michigan State University, East Lansing, MI 48824 USA (e-mail: cooloneze@gmail.com; fzpeng@msu.edu).

Color versions of one or more of the figures in this paper are available online at http://ieeexplore.ieee.org.

Digital Object Identifier 10.1109/TPEL.2016.2642050

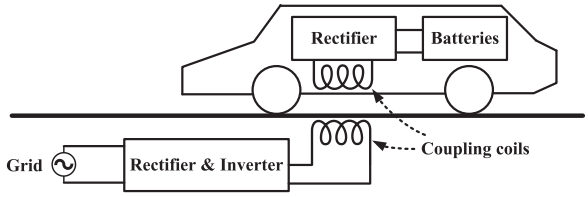

Fig. 1. Configuration of a WPT system for OLPT.

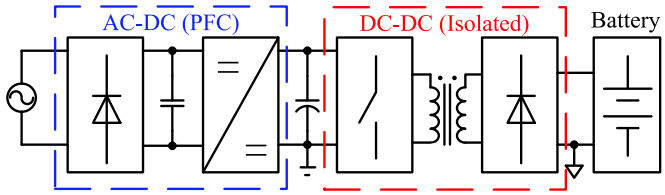

Fig. 2. Block diagram of a conventional OBC.

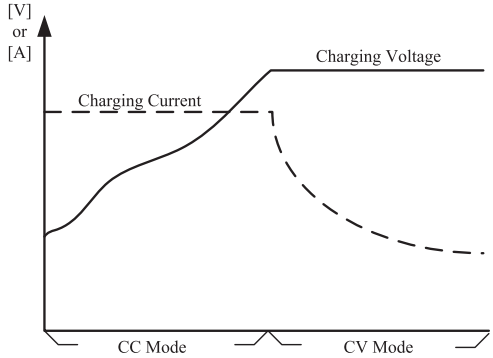

Fig. 3. OBC charging mode.

A conventional on-board battery charger (OBC) is usually a two-stage structure; a power factor correction (PFC) front-end part and a dc–dc converter part with high-frequency transformer, as shown in Fig. 2.

Load regulation function is required for the dc–dc converter as the battery charger has constant current (CC) mode and constant voltage (CV) mode, as shown in Fig. 3. In order to shorten the charging time, the people are no longer satisfied with the 3.3-kW WPT system and they are now interested in higher power (6.6 kW or more) WPT OBC systems [3]. Hence, the dc–dc converter would always try to output maximum current in CC mode without regulation. However, it should be noted

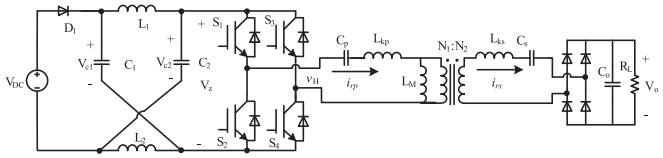

Fig. 4. Circuit schematic of the ZSRC.

that the low-medium load range in CV mode consumes 40% of the total charge time [4]. In other words, load regulation in CV mode is essential in terms of the overall performance of the OBC.

In WPT application, the series resonant dc–dc converter (SRC) is widely adopted as the dc–dc converter because of its simplicity and high efficiency [5]. An SRC, like other resonant converters, can realize load regulation by frequency modulation method (PFM). However, owing to the large ratio between the leakage inductance and magnetizing inductance (greater than 10:1) in WPT application, an SRC has a high quality factor. Small drift away from resonant frequency leads to huge drop in gain and huge increment in circulating current [6]. In [7] and [8], from Oak Ridge National Laboratory, an SRC is investigated and verified that the peak power range is broader for a given frequency band and then drops quickly outside the band. In their later work [9], they change to series–parallel configuration that has a wider plateau in the power versus frequency curve, which gives them more freedom on PFM control.

Moreover, the resonant converter is left unregulated and freewheeling with different air gaps or loads [10]–[12]. Thus, one more front-end stage is needed to regulate the dc bus voltage [13], and this front-end stage usually also performs PFC [14]–[16]. In [3], a 7-kW charger system is divided into three stages—a front-end PFC converter, a buck converter for voltage regulation, and an SRC, such that the SRC can always operate at resonant frequency with high efficiency.

Two or more stage solutions are of high cost and complicated, even though the design for each stage is simple. The overall performance may not be the best. A Z-source inverter [17], well known for its boost feature and being immune to shoot-through problem, can be applied to any kind of power conversion between dc and ac. A combination of Z-source network (ZSN) and SRC has been studied in [18]. It can improve the efficiency over a wide input voltage and load variation. Furthermore, a Z-source resonant converter (ZSRC) was proposed in [32] and proved its advantage over conventional boost PFC with a cascaded dc–dc. Fig. 4 shows the overall schematic for a ZSRC. The input diode is a silicon carbide (SiC) device with almost zero reverse recovery loss which is a previous headache for a Z-source inverter in many applications. A ZSN is placed between the input diode and the H-bridge inverter of the conventional SRC system. The original Z-source topology is chosen as it can share the input diode with the diode bridge when connecting to the ac source. The SRC converts the dc power to high frequency ac power and pass it to the secondary side. This is a single-stage solution that saves the cost and complicity.

However, the control scheme is challenged [32], as it should accomplish PFC and load regulation by controlling only four switches. And the load regulation method for the ZSRC has not been addressed. In terms of Z-source, plenty of research on the control has been done for the dc–dc converter [19]–[25]. In one switching period, the load current that the inverter draws is modeled as a CC source. However, in a resonant converter, the load current is sinusoidal over one switching period which makes everything interesting. Those conventional control schemes pay attention to the duty cycle of shoot-through state only, while the position of shoot-through state in one switching period is also crucial for the resonant converter. In [29], the shoot-through state is evenly distributed over one cycle and it results in less voltage ripple on a dc-link capacitor. A control method [30] with shoot-through state right after active state can provide soft switching at turn-on action. In this paper, for the ZSRC specifically, two constant frequency control methods—phase-shift method and pulse notch method are discussed. The pulse notch control method can theoretically regulate the load downward all the way to zero like a buck-type converter, which is a unique feature of the ZSRC. Pulse notch control is a better candidate for PFC function to achieve high power factor. A circuit description, analysis, and experimental results based on a 200-W scale-down prototype are provided in the following sections.

II. ZSRC WPT System

Different from dc/ac application, the ZSRC has more states in one switching cycle. It is important to clarify all these states to understand the ZSRC. The boost ratio of ZSN is still related to the total shoot-through state duty cycle among these states. In this section, the operation principle of the ZSRC is described based on an example of the phase-shift control method. The mechanism of pulse notch control is presented after this.

A. Operation Principle of a ZSRC WPT System

Assuming that the ZSN is symmetrical ($\mathrm{C}_1 = \mathrm{C}_2 = \mathrm{C}$, and $\mathrm{L}_1 = \mathrm{L}_2 = \mathrm{L}$) in Fig. 4, therefore, $V_{C1} = V_{C2} = V_{\mathrm{C}}$, and $v_{L1} = v_{L2} = v_L$. Also, the resonant frequency of L and C in ZSN is at least ten times smaller than the switching frequency. Hence, the ZSN inductor current and the ZSN capacitor voltage are considered constant in one switching cycle. Fig. 5 shows the conducting devices in different states—active state, shoot-through state, and zero state.

The time domain waveforms of these states are illustrated in Fig. 6. The fundamental component of H-bridge output is in phase with the primary-side current i_{rp} at resonant frequency [6], and the total time of shoot-through state (T_{st}) is evenly distributed over one switching cycle. With such phase-shift PWM modulation method, no extra switching action is needed to achieve arbitrary active state and shoot-through state duty cycle.

1) Active State: During the two active states time interval [see Fig. 5(c) and (g)], the diagonal switches are on, and the input side diode D_1 is conducting. The resonant network draws current from both the ZSN inductor and capacitor. The difference between load current (i_{rp}) and ZSN inductor current (I_L) is provided by a series connection of the two ZSN capacitor

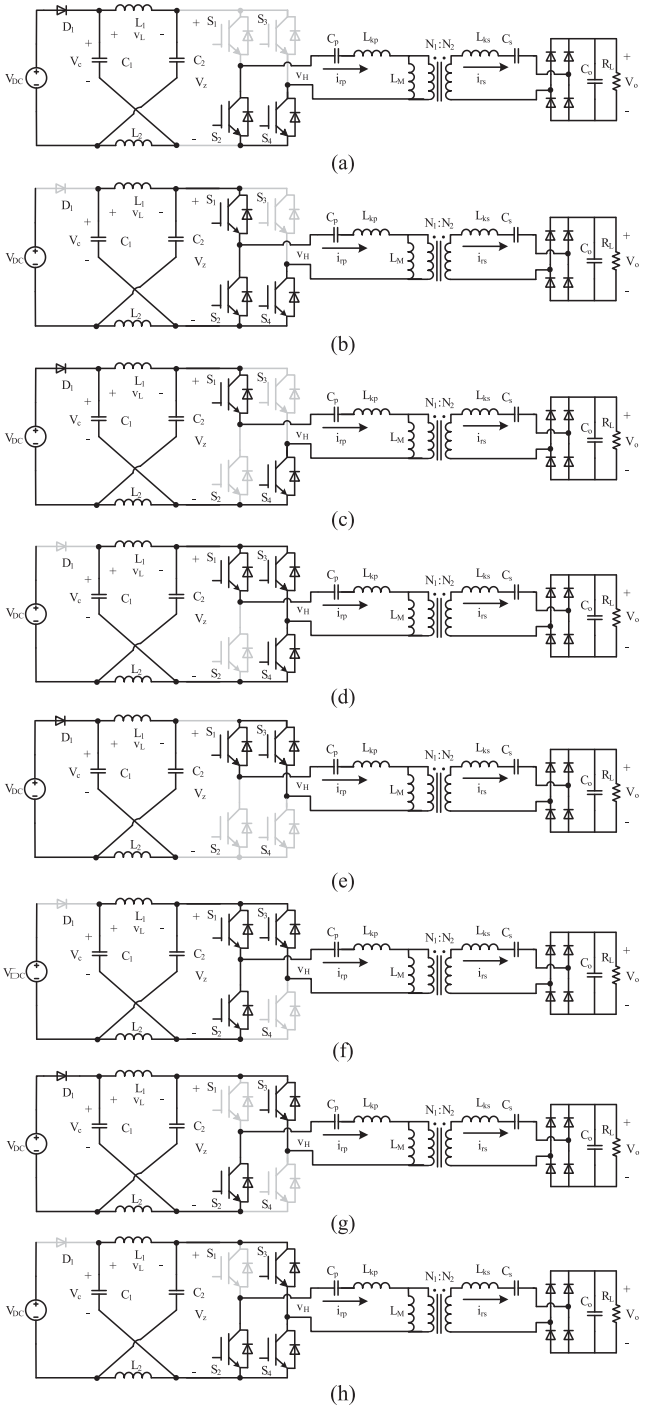

Fig. 5. ZSRC circuit diagram in different states: (a) zero state, t_0–t_1 and t_8–t_9; (b) shoot-through state, t_1–t_2; (c) active state, t_2–t_3; (d) shoot-through state, t_3–t_4; (e) zero state, t_4–t_5; (f) shoot-through state, t_5–t_6; (g) active state, t_6–t_7; and (h) shoot-through state, t_7–t_8.

and dc source [26]. The current going through the switches are only load current ($i_{\rm rp}$). The ZSN inductor voltage for this time interval is given as

$$v_L = V_{\rm DC} - V_C. \tag{1}$$

2) Shoot-Through State: Four shoot-through state's time intervals are demonstrated in Fig. 5(b), (d), (f), and (h). Three of the switches are ON. The two horizontal switches are carrying the load current and the switches in one-phase leg are carrying the ZSN inductor current. Hence, there is one switch carrying the sum of the two currents. Since the flow of ZSN inductor current is always in one direction and the load current would be bipolar, these two currents either subtract from each other or add together, contributing to the sum with their absolute value. Fortunately, phase-shift control only allows different polarity currents going through the same switch in shoot-through state. Here, the ZSN capacitors will charge ZSN inductors (this is how the ZSRC can boost the voltage) [26]. The ZSN inductor voltage for this time interval is given as

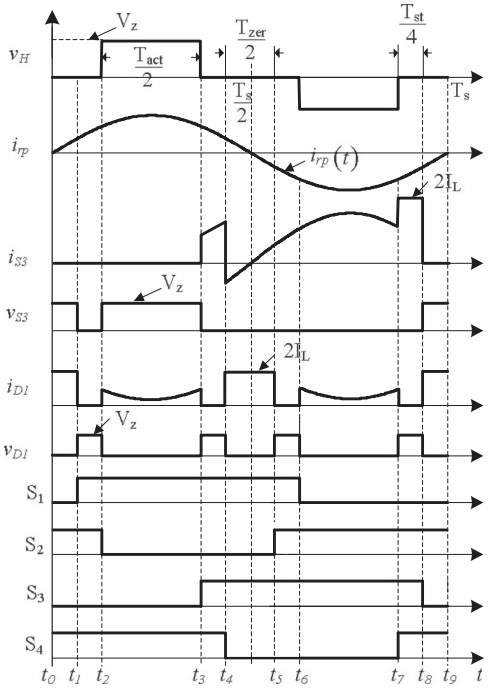

Fig. 6. Time domain waveforms for phase-shift control in the ZSRC.

$$v_L = V_C. \tag{2}$$

3) Zero State: During the zero state's time interval [see Fig. 5(a) and (e)], two horizontal switches are ON. The ZSN is isolated from the load. The load current is freewheeling and the ZSN inductors charge the ZSN capacitors. The ZSN inductors voltage for this time interval is given as

$$v_L = V_{\rm DC} - V_C. \tag{3}$$

To derive the expression for the shoot-through state duty cycle, one can use voltage second balance across the ZSN inductor over one switching period. Therefore, by using (1)–(3), we have

$$\frac{T_{\rm act}}{T_S}(V_{\rm DC}-V_C)+\frac{T_{\rm st}}{T_S}V_C+\left(1-\frac{T_{\rm act}}{T_S}-\frac{T_{\rm st}}{T_S}\right)(V_{\rm DC}-V_C)=0 \tag{4}$$

where the switching period is defined as $T_{\rm s} = T_{\rm act} + T_{\rm st} + T_{\rm zer}$. The active state duty cycle is defined as $D_{\rm act} = T_{\rm act}/T_s$,

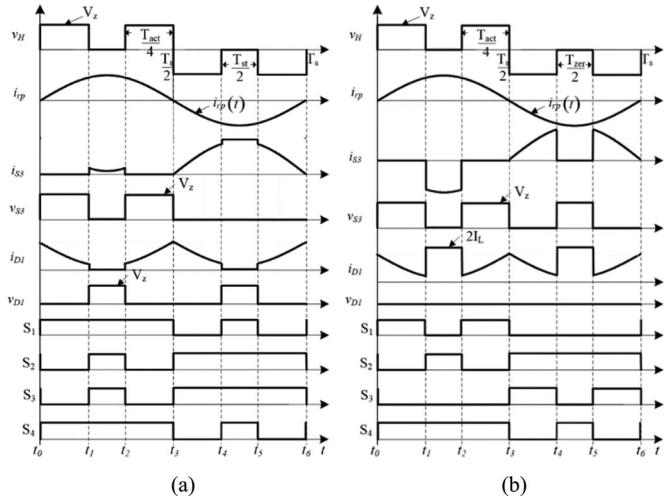

Fig. 7. Time domain waveforms for pulse notch control in the ZSRC. (a) Shoot-through notch and (b) zero notch.

and the shoot-through state duty cycle is defined as $D_{\rm st} = T_{\rm st}/T_s$.

By solving (4), we have

$$V_C = \frac{1 - D_{\rm st}}{1 - 2D_{\rm st}} V_{\rm DC} \tag{5}$$

$$D_{\rm st} = \frac{V_z - V_{\rm DC}}{2V_z} = \frac{V_C - V_{\rm DC}}{2V_C - V_{\rm DC}} \tag{6}$$

and

$$V_z = \frac{V_{DC}}{1 - 2D_{\rm st}}. \tag{7}$$

The relationship in (6) gives us a hint that the voltage on the ZSN capacitor is irrelevant to active state duty cycle $D_{\rm act}$.

These three states are all the possible states in the ZSRC. Different allocations of these three states along one switching period would generate different load regulation characteristics. In next section, pulse notch control will be presented.

B. Mechanism of Pulse Notch Control for a ZSRC WPT System

In phase-shift control, different phase shifts actually generate different amplitudes of the fundamental component at switching frequency. Thus, controlling a notch width shares a similar idea, as Fig. 7 shows. Pulse notch control is usually used in a three-phase system [27], as it does not damage the symmetry of the three-phase system. In the case of a single-phase ZSRC, this notch can be either shoot-through state or zero state, which is illustrated in Fig. 7(a) and (b), respectively. Fig. 7 shows less state change than Fig. 6, and the detail description of each state is not repeated here.

The shoot-through notch will increase the output power as the boost from the shoot-through state surpasses the loss in active state. The mathematic explanation will be expanded in the next section. The original control signals (S10, S20, S30, and S40) come from a 50% duty cycle with constant frequency PMW signal. Apart from that, one control logic block [see Fig. 8(a)] is inserted between these original signals and gate signals (S1, S2, S3, and S4). When the shoot-through control signal $S_{\rm sh}$ is high, all the gate signals are forced high as t_1–t_2 and t_4–t_5 in Fig. 7(a). The shoot-through notch is placed in the middle of active state for the sake of symmetry.

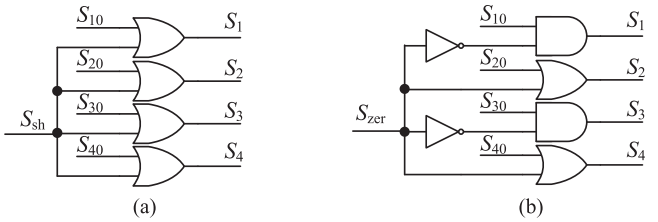

Fig. 8. Control logic block inserted for pulse notch control. (a) Shoot-through notch and (b) zero notch.

Fig. 7(b) shows another kind of notch. Zero state is filled in the middle of active state. Zero notch will help regulating the output power downward. The control concept is similar to the previous one. The original control signals (S10, S20, S30, and S40) come from a 50% duty cycle with constant frequency PMW signal. One control logic block [see Fig. 8(b)] is inserted between these original signals and gate signals (S1, S2, S3, and S4). When the zero control signal $S_{\rm zer}$ is high, S2 and S4 are forced high and S1 and S3 are forced low. For simplicity, here, only the zero state with two bottom switches is utilized. It is worth noting that S3 and S4 have the same current waveform with notch, as shown in Fig. 7(b). And, S1 and S2 have half-sinusoidal current waveform without notch because of the asymmetric control.

This pulse notch control actually doubles the switching frequency, but the excitation frequency for the resonant network remains the same.

III. Load Regulation for a ZSRC WPT System

As mentioned in the previous section, the load current is limited by the ZSN inductor current in active state. As the load current is sinusoidal, the peak value of the load current may easily reach the limitation ($2I_L$) and the output voltage v_H will collapse, which is called the discontinuous mode. Based on continuous mode or discontinuous mode of output voltage, this section is organized as follows: Section III-A describes the output power regulation under continuous mode; in Section III-B, the boundary of discontinuous mode will be developed; the power correction for discontinuous mode and the power loss analysis have been discussed in Sections III-C and III-D, respectively.

A. Output Power Regulation for a ZSRC WPT System

In order to get the output power derivation, the WPT system can be simplified as one voltage source v_H and a resonant network with all the parameters reflected to primary side. In Fig. 9, the voltage source v_H is the output of H-bridge and it contains different frequency components. $R_{\rm ac}$ is the ac equivalent resistor that can be expressed as

$$R_{\rm ac} = 8R_o/\pi^2 \tag{8}$$

Z_p and Z_s are primary-side impedance and secondary-side impedance, respectively. Z_o represents the output impedance.

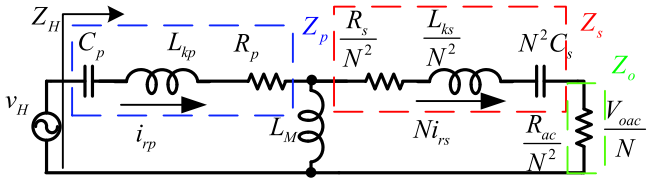

Fig. 9. Simplified circuit of the resonant network.

N is the turn ratio. The impedance from the output terminals of H-bridge (Z_H) is given as

$$Z_H(\omega) = Z_p(\omega) + \frac{(Z_s(\omega) + Z_o) \cdot j\omega L_M}{j\omega L_M + Z_s(\omega) + Z_o}. \tag{9}$$

Also, at resonant frequency ω_0, with certain compensation [6], the impedance Z_H is purely resistive (R_H). We have

$$R_H = Z_H(\omega_0) = R_p + \frac{(\omega_0 L_M)^2}{(R_{\rm ac} + R_s)/N^2}. \tag{10}$$

In the WPT system, only the resonant frequency component is carrying power, while other frequency components are greatly attenuated by the resonant network. Therefore, the resonant component of $v_H(t)$ is given as

$$v_{H,1} = \frac{\sqrt{2}}{T_s}\int_0^{T_s} v_H(\tau)\sin(\omega_s\tau)d\tau. \tag{11}$$

Based on different time domain waveforms of different control methods in Figs. 6 and 7, the integration of active state in (11) will give us

$$v_{H,1} = \frac{2\sqrt{2}}{T_s}\int_{\frac{T_s}{4}-\frac{T_{\rm act}}{4}}^{\frac{T_s}{4}+\frac{T_{\rm act}}{4}} V_z\sin(\omega_s\tau)d\tau = \frac{2\sqrt{2}V_{\rm in}}{(1-2D_{\rm st})T_s} \times\int_{\frac{T_s}{4}-\frac{T_{\rm act}}{4}}^{\frac{T_s}{4}+\frac{T_{\rm act}}{4}} \sin\left(\frac{2\pi}{T_s}\tau\right)d\tau = \frac{2\sqrt{2}V_{\rm in}}{\pi(1-2D_{\rm st})}\sin\left(\frac{\pi D_{\rm act}}{2}\right) \tag{12}$$

and

$$v_{H,1} = \frac{4\sqrt{2}}{T_s}\int_0^{\frac{T_{\rm act}}{4}} V_z\sin(\omega_s\tau)d\tau = \frac{2\sqrt{2}V_{\rm in}}{\pi(1-2D_{\rm st})} \times\left[1-\cos\left(\frac{\pi D_{\rm act}}{2}\right)\right]. \tag{13}$$

Formula (12) is for phase-shift control and (13) is for pulse notch control. Then, the output power from H-bridge is

$$P_H = v_{H,1}^2/R_H. \tag{14}$$

As the resonant network is all passive components and they are all linear, the final output power P_o is proportional to P_H. For the sake of examining output power regulation, a unified expression for both control methods is enough. We have

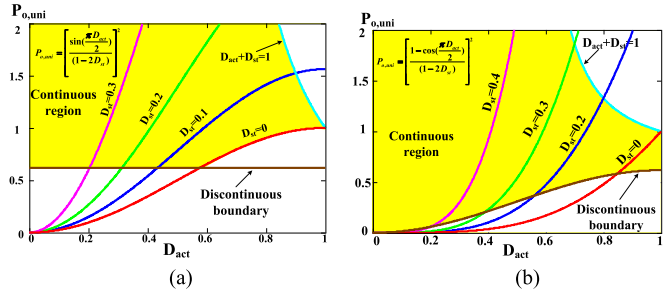

Fig. 10. Unified power curves with different control variables. (a) Phase-shift control and (b) pulse notch control.

$$P_{o,\rm uni} = \frac{P_H}{P_{H,\rm uni}} = \frac{\left[\frac{2\sqrt{2}V_{\rm in}}{\pi(1-2D_{\rm st})}\sin\left(\frac{\pi D_{\rm act}}{2}\right)\right]^2/R_H}{P_{H,\rm uni}} = \frac{8V_{\rm in}^2/\left(\pi^2 R_H\right)}{P_{H,\rm uni}}\left[\frac{\sin(\pi D_{\rm act}/2)}{(1-2D_{\rm st})}\right]^2 = \left[\frac{\sin(\pi D_{\rm act}/2)}{(1-2D_{\rm st})}\right]^2 \tag{15}$$

and

$$P_{o,\rm uni} = \left[\frac{1-\cos(\pi D_{\rm act}/2)}{(1-2D_{\rm st})}\right]^2 \tag{16}$$

where $P_{H,\rm uni}$ is the base value that equals $8V_{\rm in}^2/(\pi^2 R_H)$. These two unified power expression are plotted in Fig. 10(a) and (b), respectively. When the shoot-through duty cycle $D_{\rm st}$ is zero and active state duty cycle $D_{\rm act}$ is 1, both of them generate one unit of power. They are actually the same with 50% duty cycle. From this unit power point upward, it needs certain amount of $D_{\rm st}$ to boost the power for both control methods. From this point downward, $D_{\rm act}$ is the leading role of regulation.

The upward difference between these two control methods is the slope of the full duty cycle boundary ($D_{\rm act} + D_{\rm st} = 1$). Phase-shift control has a higher slope which means the same amount of $D_{\rm st}$ will generate more power. Hence, for the same output power (larger than 1), phase-shift control would have less voltage stress on the switch compared to the other one. Also, phase-shift control can work in the entire continuous region, while the pulse notch control can only work at the downward curve where $D_{\rm st} = 0$. In order to work at the entire continuous region for pulse notch control, it needs to combine shoot-through notch and zero notch in one switching cycle, which increases the switching frequency a lot and is not preferred. However, the continuous region can reach zero in pulse notch control, while the other one is clamped at a certain point. This important characteristic of discontinuous boundary will be discussed in next section. For both control schemes, less $D_{\rm st}$ results in less voltage stress on the switches, thus the right-hand-side boundary is more preferred in the both control schemes.

B. Discontinuous Mode Boundary for a ZSRC WPT System

Discontinuous mode happens when the load current reaches twice the ZSN inductor current limitation. In this section, the

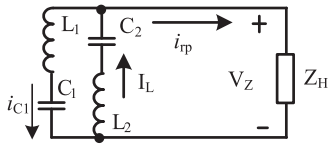

Fig. 11. Equivalent circuit in output voltage discontinuous mode.

boundary of discontinuous mode will be developed and the working state in discontinuous mode will be analyzed next.

In order to get the peak value of load current, P_H in (14) is revised as

$$P_H = \frac{2}{T_s}\int_{\frac{T_s}{4}-\frac{T_{\rm act}}{4}}^{\frac{T_s}{4}+\frac{T_{\rm act}}{4}} V_z \hat{i}_{rp}\sin(\omega_s\tau)d\tau \tag{17}$$

and

$$P_H = \frac{4}{T_s}\int_{0}^{\frac{T_{\rm act}}{4}} V_z \hat{i}_{rp}\sin(\omega_s\tau)d\tau. \tag{18}$$

The variable $\hat{i}_{\rm rp}$ is the peak value of the load current. In phase-shift control, the converter enters discontinuous mode when $\hat{i}_{\rm rp}$ reaches $2I_{\rm L}$, as Fig. 6 shows. In contrast, for pulse notch control, the converter enters discontinuous mode when $\hat{i}_{rp}\sin(\pi D_{\rm act}/2)$ reaches $2I_L$, as Fig. 7 shows. Further developing (17) and (18), we have

$$\hat{i}_{rp} = \frac{P_H}{V_{\rm in}}\cdot\frac{\pi(1-2D_{\rm st})}{2\sin(\pi D_{\rm act}/2)} \tag{19}$$

and

$$\hat{i}_{rp}\sin(\pi D_{\rm act}/2) = \frac{P_H}{V_{\rm in}}\cdot\frac{\pi(1-2D_{\rm st})\sin(\pi D_{\rm act}/2)}{2\left[1-\cos(\pi D_{\rm act}/2)\right]}. \tag{20}$$

The ZSN inductor current is the same as the input current [28], assuming no loss in the ZSN. One can obtain

$$I_L = P_{\rm in}/V_{\rm in} = P_H/V_{\rm in}. \tag{21}$$

From (19)–(21), we can derive the relationship between $D_{\rm st}$ and $D_{\rm act}$ when the load current reaches $2I_L$. This relationship is plotted in terms of unified power in Fig. 10. The discontinuous boundary is flat in phase-shift control while it declines in pulse notch control. If the converter is always working in the continuous region, pulse notch control has the ability to regulate the load down to zero theoretically. However, due to the complexity of controlling $D_{\rm st}$ in the downward curve for pulse notch control, discontinuous mode is unavoidable at light load conditions.

C. Power Correction in Discontinuous Mode for a ZSRC WPT System

In discontinuous mode, the load current $i_{\rm rp}$ is clamp at $2I_L$. The input diode is OFF and an equivalent circuit is shown in Fig. 11. The impedance of the resonant network is much smaller (at least ten times smaller) than the ZSN impedance, thus the voltage drop in resonant network (V_z) is almost zero. At the same time, the ZSN inductor's current is charging the ZSN capacitor, which is exactly the same as the shoot-through state. The only difference is that the shoot-through current is bypassed by the switch or it flows through the resonant network. Discontinuous mode will decrease the active state duty cycle which affects the output power.

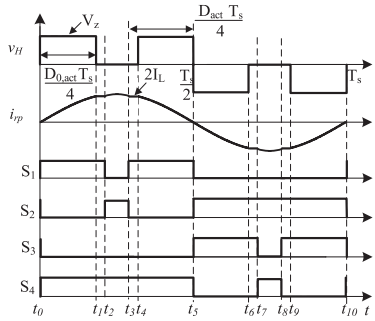

Fig. 12. Time domain waveforms in discontinuous mode for pulse notch control.

When the discontinuous mode happens, the resonant current is clamped as $2I_L$ and part of the active state is lost. Fig. 12 shows an example of pulse notch control in discontinuous mode. The zero notches are from t_2 to t_3 and t_7 to t_8 in Fig. 12, but part of the active state is occupied by shoot-through state in discontinuous mode. The actual active state duty cycle is defined as $D_{0,\rm act}$, and the command of active state duty cycle is still $D_{\rm act}$.

The fundamental component of v_H is

$$\begin{aligned} v_{H,1} &= \frac{4\sqrt{2}}{T_s}\int_0^{\frac{T_{\rm act}}{4}} V_z\sin(\omega_s\tau)d\tau \\ &= \frac{2\sqrt{2}V_z}{\pi}\left[1-\cos\left(\frac{\pi D_{0,\rm act}}{2}\right)\right]. \end{aligned} \tag{22}$$

The dc output voltage V_z is determined by average shoot-through duty cycle as

$$V_z = \frac{V_{\rm in}}{1-2D_{\rm st}} = \frac{V_{\rm in}}{1-2\cdot(D_{\rm act}-D_{0,\rm act})}. \tag{23}$$

From (22) and (23), we have the unified power expression as

$$P_{o,\rm uni} = \left[\frac{1-\cos(\pi D_{0,\rm act}/2)}{(1-2D_{\rm act}+2D_{0,\rm act})}\right]^2. \tag{24}$$

$D_{0,\rm act}$ is a variable that depends on $D_{\rm act}$, and their relationship can be derived when $\hat{i}_{rp}\sin(\pi D_{0,\rm act}/2)$ reaches $2I_L$, as Fig. 12 shows. We have

$$\frac{\pi(1-2D_{\rm act}+2D_{0,\rm act})\sin(\pi D_{0,\rm act}/2)}{2\left[1-\cos(\pi D_{0,\rm act}/2)\right]} = 2. \tag{25}$$

However, (25) is a transcendental equation and it can only be solved by numerical calculation. This discontinuous unified power curve is plotted in Fig. 13(b). The load can be regulated all the way down to zero as the black dash curve shows.

Following the same procedure, the power correction for phase-shift control is calculated and plotted in Fig. 13(a). However, its transcendental equation only has solution when $D_{\rm act}$ is larger than 0.5. This means phase-shift control cannot regulate the load down to zero, or the output voltage v_H is no longer a quasi-square waveform. To control the output power in continuous mode, one can follow (15) and (16). However, there is

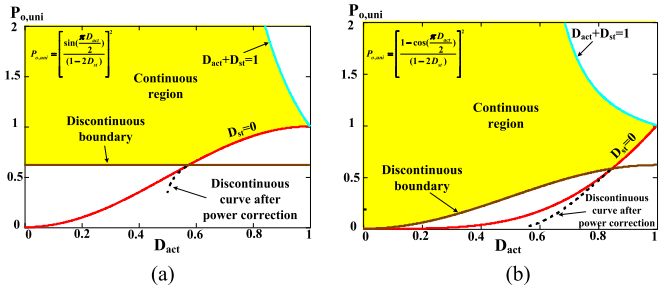

Fig. 13. Unified power curves with power correction. (a) Phase-shift control and (b) pulse notch control.

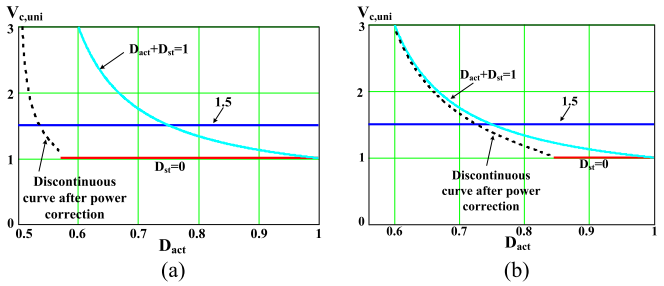

Fig. 14. Unified Z-source capacitor voltage curves for different loads corresponding to Fig. 13. (a) Phase-shift control and (b) pulse notch control.

no mathematical expression for discontinuous mode. An output power look-up table should be made offline as the dash line shown in Fig. 13. By searching the lookup table, the controller can give the actual command ($D_{\rm act}$) according to the power required.

D. Power Loss in a ZSRC WPT System

Different from the traditional SRC system, ZSN brings an extra shoot-through state to the H-bridge. The shoot-through state will affect both switching loss and conduction loss for the switches, especially when the ZSRC is doing hard switching.

1) Switching Loss for H-bridge: Both control schemes experience hard switching between different states. The switching loss depends on the voltage stress and current stress at the switching moment. For the ZSRC, the voltage stress for the H-bridge is constant ($2V_c - V_{\rm DC}$) over one switching cycle and only related to shoot-through duty cycle.

A unified Z-source capacitor voltage ($V_{c,\rm uni}$) curve for both control methods is shown in Fig. 14. The base is $V_{\rm DC}$. $V_{c,\rm uni}$ increases a lot with either heavy load in light blue curve or light load in dash line. It is also reported [31] that the Z-source inverter has advantage over the boost converter plus inverter with boost ratio lower than 2, which is 1.5 for the Z-source capacitor. To avoid high voltage stress on the device, the ZSRC should be designed in the region lower than 1.5 in Fig. 14 for most load conditions.

On the other hand, the current stress for switching action depends on the instantaneous current value and the switching between specific states. Table I shows the instantaneous current difference expressions between different states during the switching action.

TABLE I
INSTANTANEOUS CURRENT DIFFERENCE BETWEEN DIFFERENT STATES

	Active state	Zero state	Shoot-through state
Active state	0	$\hat{i}_{rp}\lvert\sin(\theta)\rvert$	$2I_L - \hat{i}_{rp}\lvert\sin(\theta)\rvert$
Zero state	$\hat{i}_{rp}\lvert\sin(\theta)\rvert$	0	$2I_L$
Shoot-through state	$2I_L - \hat{i}_{rp}\lvert\sin(\theta)\rvert$	$2I_L$	0

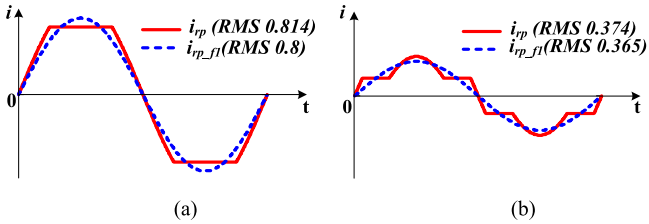

Fig. 15. Primary-side resonant current $i_{\rm rp}$ in deep discontinuous mode. (a) Phase-shift control with $D_{\rm act} = 0.5$ and (b) pulse notch control with $D_{\rm act} = 0.56$.

For both control methods, the upward section (larger than 1) on power curve only has active state and shoot-through state. The switching action takes place at the peak of $i_{\rm rp}$ for pulse notch control, while i_{rp} is zero for phase-shift control. Therefore, pulse notch control has soft switching at the region slightly larger than 1 unit power.

When the shoot-through duty cycle is zero, the ZSRC is reduced to a traditional SRC. As the active state duty cycle decreases from 1, phase-shift control has soft switching while pulse notch control experiences hard switching at peak current. As the load further decreases, both control schemes enter discontinuous mode. Phase-shift control still has the same situation as above, since the discontinuous behavior happens in the middle of active state without any switching action. However, for pulse notch control, the discontinuous mode appears at the edge of active state and results in the switching action between shoot-through state and zero state. This is the worst case and is given in Table I, which is a drawback of pulse notch control.

2) Conduction Loss for the Resonant Network: As the simplified circuit shown in Fig. 9, the ZSN does not affect the resonant network characteristic. The output of H-bridge can still be modeled as a voltage source. With this voltage source, the resonant current only relates to the resonant network and the load. Therefore, the conduction loss caused by the primary-side resonant current $i_{\rm rp}$ is the same as the traditional H-bridge SRC system in continuous mode. As there is distortion of $i_{\rm rp}$ in discontinuous mode, the RMS value of $i_{\rm rp}$ may change and induce more conduction loss on H-bridge and winding.

Fig. 15 shows the distorted $i_{\rm rp_{f1}}$ in deep discontinuous mode for both control methods. The fundamental component ($i_{\rm rpf1}$) of $i_{\rm rp}$ carries the power to the secondary side, while other harmonics circulate in primary side and cause extra conduction loss. One can observe that even in the deepest discontinuous mode, the rms values for $i_{\rm rp_{f1}}$ are 1.8% (phase-shift control) and 2.5% (pulse notch control) higher than that of $i_{\rm rpf1}$. Hence, the distortion in discontinuous mode has limited effect on the conduction

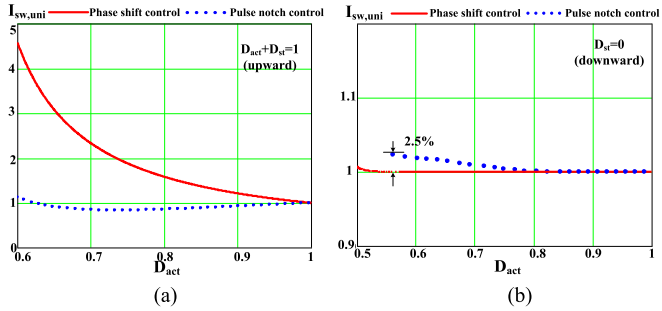

Fig. 16. Unified switch current curves for different loads corresponding to Fig. 15. (a) For power curve larger than unit power (upward) and (b) for power curve smaller than unit power (downward).

loss. For simplification, this distortion is not considered into any theoretical calculation.

3) Conduction Loss for H-Bridge: As given in Table I, the ZSRC switches will carry extra shoot-through current ($2I_L$) compared to that of traditional SRC. The switch current's rms value is the integration of i_{s3} from Figs. 6 and 7, respectively, and its expression is given as

$$i_{s3,\mathrm{RMS}}(D_{\mathrm{st}}, D_{\mathrm{act}}) = \sqrt{(1/T_s)\int_0^{T_s} i_{s3}(D_{\mathrm{st}}, D_{\mathrm{act}}, t)^2 dt}. \tag{26}$$

This switch current's rms value is converted to a unified value ($I_{\mathrm{sw,uni}}$) with the resonant current's fundamental component as the base. One can obtain

$$I_{\mathrm{sw,uni}} = \frac{i_{s3,\mathrm{RMS}}(D_{\mathrm{st}}, D_{\mathrm{act}})}{\sqrt{(1/T_s)\int_0^{\frac{T_s}{2}} i_{rp\_f1}(D_{st}, D_{\mathrm{act}})^2 dt}}. \tag{27}$$

As each switch in one-phase leg conducts 50% of time, the base current only considers the integration of half-cycle in (27). Fig. 16 shows the unified switch current curves for different loads corresponding to Fig. 15. In Fig. 16(a), the shoot-through state is dominating and leads to extra loss for phase-shift control. That is because the shoot-through state happens at the absolute minimum point of the resonant current. In contrast, the shoot-through notch locates at the absolute maximum point of the resonant current, such that the extra current stress is limited. Also, pulse notch control allows all four switches to turn ON and share the shoot-through current, which further helps the conduction loss. As Fig. 16(a) shows, the $I_{\mathrm{sw,uni}}$ of pulse notch control even has values less than 1, and this implies that it has less conduction loss with ZSN compared to the traditional SRC.

Fig. 16(b) shows the unified switch current curves for the power less than $P_{H,\mathrm{uni}}$ (downward). In continuous mode, the H-bridge actually is a current chopper. As the switch action is symmetric, the current's rms value is the same as one unit. When the ZSRC enters discontinuous mode, there is current distortion as described above. However, each phase leg still behaves as a current chopper and there is limited rms increment from the distorted current in deep discontinuous mode.

Since the input diode is an SiC device, it has negligible switching loss. Its conduction loss depends on the rms value of input current and is almost irrelevant to control schemes.

TABLE II
PROTOTYPE PARAMETERS AND VALUES

Parameters	Value	Parameters	Value
Input voltage (V_{dc})	33 V	Primary-side compensating capacitor (C_p)	180 nF
Output	88 V/2.28 A	Primary-side leakage inductance (L_{kp})	0.415 mH
Resonant frequency	18.2 kHz	Magnetizing inductance (L_M)	61.87 μH
Transformer turns ratio	15:20	Secondary side leakage inductance (L_{ks})	1.07 mH
ZSN capacitors (C_1, C_2)	4.7 mF	Secondary-side compensating capacitor (C_s)	65.8 nF
ZSN inductors (L_1, L_2)	1 mH	Output filter capacitor (C_o)	1 mF
H-bridge	6MBP100VEA120	Output rectifier	15ETH03PBF
Input diode (SiC)	GHXS020A060S		

The experimental waveforms of both control methods will be presented in next section.

IV. EXPERIMENTAL RESULTS

The analysis and design guidelines of the proposed ZSRC system are verified based on a 200 W scale-down prototype, whose parameters are summarized in Table II.

The full-bridge output voltage v_{H} and primary-side resonant current i_{rp} for both control methods are shown in Fig. 17. The ZSRC is working at full load, half-load, and 1/4 load, respectively, with constant output voltage. Full load is set at a point larger than $P_{H,\mathrm{uni}}$. At full load in Fig. 17(a) and (b), we can observe that the dc bus voltage V_z is higher in pulse notch control compared to phase-shift control. That is, because the power curve for phase-shift control is steeper than pulse notch control when regulating the power upward. Pulse notch control needs more shoot-through duty cycle to maintain the same output power as phase-shift control does. In terms of voltage stress on the switches, phase-shift control is better in the region larger than $P_{H,\mathrm{uni}}$.

At half-load in Fig. 17(c) and (d), both control methods show similar performance in the light discontinuous mode. Phase-shift control would have extra shoot-through state in the middle of active state. The extra shoot-through state in pulse notch control merge with zero state, such that one cannot tell the difference in v_H.

As the load further decreases, as shown in Fig. 17(e) and (f), phase-shift control has a very high voltage spike around 125 V while the pusle notch control only has a peak voltage value around 60 V. For theoretical analysis, there is no solution for phase-shift control's transcendental equation at light load in Fig. 13(a), which means the waveform of phase-shift control has huge distortion and is uncontrollable. Drawing power under such a condition results in high voltage spike. On the other hand, pulse notch control maintains quite good quality waveforms as expected.

Fig. 18 shows the unified power curve for both control methods. Expermental results match with calculation very well for pusle notch control as there is almost no distortion in deep

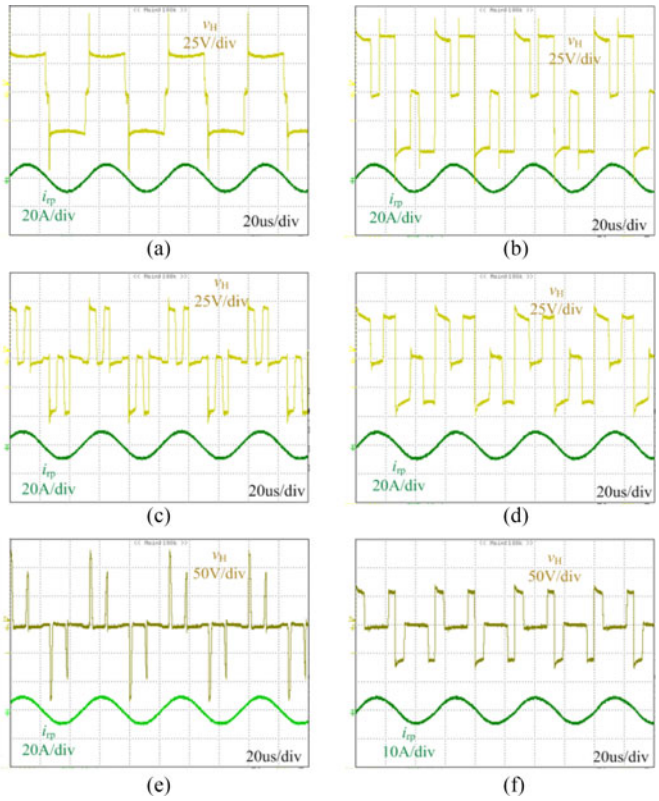

Fig. 17. Experimental waveforms of v_H and $i_{\rm rp}$ ($V_o = 88$ V, full load @$R_L = 40\,\Omega$, half-load @ $R_L = 80\,\Omega$, and 1/4 load @$R_L = 160\,\Omega$). (a) Full load, phase-shift control command $D_{\rm act} = 0.9$, $D_{\rm st} = 0.1$. (b) Full load, pulse notch control command $D_{\rm act} = 0.78$, $D_{\rm st} = 0.22$. (c) Half-load, phase-shift control command $D_{\rm act} = 0.53$, $D_{\rm st} = 0$. (d) Half-load, pulse notch control command $D_{\rm act} = 0.79$, $D_{\rm st} = 0$. (e) 1/4 load, phase-shift control command $D_{\rm act} = 0.47$, $D_{\rm st} = 0$. (f) 1/4 load, pulse notch control command $D_{\rm act} = 0.66$, $D_{\rm st} = 0$.

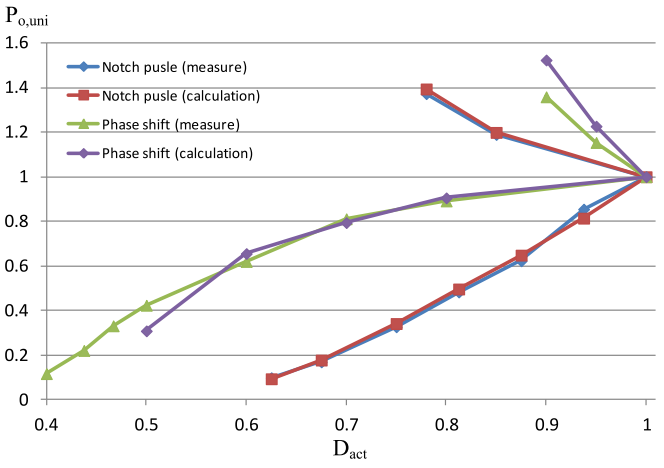

Fig. 18. Experimental unit power curve ($R_L = 40\,\Omega$, open loop, unit power = 150 W)

discontinuous mode. For phase-shift control, it is predictable with continuous mode below $P_{H,\rm uni}$ and light discontinuous mode. As the upward power curve for phase-shift control is steep when regulating the power upward, a small error in control command would be amplified. Gate signal delay difference between different switches or the turn-on and turn-off transient may cause the partial loss in shoot-through state duty cycle. These are the problems that phase-shift control has, while pulse notch control matches theoretical analysis quite well.

V. Conclusion

This paper focuses on the load regulation methods in an SiC-based ZSRC for WPT application. Two constant frequency control methods, phase-shift control and pulse notch control, are presented with comparison on load regulation performance. Phase-shift control is easier in implementation but it suffers from high distortion at light load in discontinuous mode. On the other hand, pulse notch control is more predictable than phase-shift control over the entire load range. However, both control methods are doing hard switching, which is a drawback for the ZSRC. Fortunately, it does not have much switching loss since the switching frequency is less than 20 kHz in this WPT application. Experimental results based on a 200-W scale-down prototype with the ZSRC are presented. For future work, these two control methods can be applied for PFC and load regulation at the same time in the ZSRC that leads to a single-stage solution for an EV charger. Pulse notch control is a better candidate for PFC function to achieve high power factor. Also, soft switching techniques will be examined on the ZSRC.

References

[1] M. Yilmaz and P. T. Krein, "Review of battery charger topologies, charging power levels, and infrastructure for plug-in electric and hybrid vehicles," *IEEE Trans. Power Electron.*, vol. 28, no. 5, pp. 2151–2169, May 2013.

[2] F. Musavi, M. Edington, and W. Eberle, "Wireless power transfer: A survey of EV battery charging technologies," in *Proc. 2012 IEEE Energy Convers. Congr. Expo.*, Sep. 15–20, 2012, pp. 1804–1810.

[3] J. Deng, F. Lu, L. Siqi, T.-D. Nguyen, and C. Mi, "Development of a high efficiency primary side controlled 7 kW wireless power charger," in *Proc. 2014 IEEE Int. Elect. Veh. Conf.*, Dec. 17–19, 2014, pp. 1–6.

[4] B. Y. Chen and Y. S. Lai, "New digital-controlled technique for battery charger with constant current and voltage control without current feedback," *IEEE Trans. Ind. Electron.*, vol. 59, no. 3, pp. 1545–1553, Mar. 2012.

[5] S. Y. Choi, B. W. Gu, S. Y. Jeong, and C. T. Rim, "Advances in wireless power transfer systems for roadway-powered electric vehicles," *IEEE J. Emerg. Sel. Topics Power Electron.*, vol. 3, no. 1, pp. 18–36, Mar. 2015.

[6] H. Zeng, S. Yang, and F. Peng, "Wireless power transfer via harmonic current for electric vehicles application," in *Proc. IEEE Appl. Power Electron. Conf. Expo.*, Mar. 15–19, 2015, pp. 592–596.

[7] O. C. Onar, J. M. Miller, S. L. Campbell, C. Coomer, C. P. White, and L. E. Seiber, "Oak Ridge National Laboratory wireless power transfer development for sustainable campus initiative," in *Proc. IEEE Transp. Electrif. Conf. Expo.*, Dearborn, MI, USA, Jun. 2013, pp. 1–8.

[8] J. M. Miller and O. C. Onar, "Short course on wireless power transfer (WPT) systems," in *Proc. IEEE Transp. Electrif. Conf. Expo.*, Dearborn, MI, USA, Jun. 2013, pp. 1–4.

[9] G. A. Covic, J. T. Boys, M. L. G. Kissin, and H. G. Lu, "A three-phase inductive power transfer system for roadway-powered vehicles," *IEEE Trans. Ind. Electron.*, vol. 54, no. 6, pp. 3370–3378, Dec. 2007.

[10] M. Kwon, S. Jung, and S. Choi, "A high efficiency bi-directional EV charger with seamless mode transfer for V2G and V2H application," in *Proc. 2015 IEEE Energy Convers. Congr. Expo.*, Montreal, QC, Canada, 2015, pp. 5394–5399.

[11] S. C. Moon, B.-C. Kim, S.-Y. Cho, C.-H. Ahn, and G.-W. Moon, "Analysis and design of a wireless power transfer system with an intermediate coil for high efficiency," *IEEE Trans. Ind. Electron.*, vol. 61, no. 11, pp. 5861–5870, Nov. 2014.

[12] Y. Iga, H. Omori, T. Morizane, N. Kimura, Y. Nakamura, and M. Nakaoka, "New IPT-wireless EV charger using single-ended quasi-resonant converter with power factor correction," in *Proc. 2012 Int. Conf. Renewable Energy Res. Appl.*, Nov. 11–14, 2012, pp. 1–6.
[13] H. Ishihara *et al.*, "A voltage ratio-based efficiency control method for 3 kW wireless power transmission," in *Proc. 29th Annu. IEEE Appl. Power Electron. Conf. Expo., 2014*, Mar. 16–20, 2014, pp. 1312–1316.
[14] O. C. Onar, J. M. Miller, S. L. Campbell, C. Coomer, Cliff. P. White, and L. E. Seiber, "A novel wireless power transfer for in-motion EV/PHEV charging," in *Proc. 2013 28th Annu. IEEE Appl. Power Electron. Conf. Expo.*, pp. 3073–3080, Mar. 17–21, 2013.
[15] J. Huh, W. Lee, G.-H.Cho, B. Lee, and C.-T. Rim, "Characterization of novel inductive power transfer systems for on-line electric vehicles," in *Proc. 2011 26th Annu. IEEE Appl. Power Electron. Conf. Expo.*, Mar. 6–11, 2011, pp. 1975–1979.
[16] S. Kiratipongvoot, Z. Yang, C. K. Lee, and S. S. Ho, "Design a high-frequency-fed unity power-factor AC-DC power converter for wireless power transfer application," in *Proc. 2015 IEEE Energy Convers. Congr. Expo.*, Montreal, QC, Canada, 2015, pp. 599–606.
[17] F. Z. Peng, "Z-source inverter," *IEEE Trans. Ind. Appl.*, vol. 39, no. 2, pp. 504–510, Mar./Apr. 2003.
[18] H. Cha,, F. Z. Peng, and D. W. Yoo, "Z-source resonant DC-DC converter for wide input voltage and load variation," in *Proc. 2010 Int. Power Electron. Conf.*, 2010, pp. 995–1000.
[19] Y. P. Siwakoti and G. Town, "Improved modulation technique for voltage fed quasi-Z-source DC/DC converters," in *Proc. IEEE Appl. Power Electron. Conf. Expo.*, Mar. 2014, pp. 1973–1978.
[20] Y. P. Siwakoti, F. Blaabjerg, P. C. Loh, and G. E. Town, "A high gain quasi-Z-source push-pull isolated DC/DC converter," *IET Power Electron,* vol. 7, no. 9, pp. 2387–2395, 2014.
[21] M. K. Nguyen, Q. D. Phan, V. N. Nguyen, Y. C. Lim, and J. K. Park, "Trans-Z-source-based isolated DC-DC converters," in *Proc. 2013 IEEE Int. Symp. Ind. Electron.*, May 2013, pp. 1–6.
[22] F. Evran and M. T. Aydemir, "Z-source-based isolated high step-up converter," *IET Power Electron.*, vol. 6, no. 1, pp. 117–124, 2013.
[23] X. Fang and X. Ji, "Bidirectional power flow Z-source DC/DC converter," in *Proc. Veh. Power Propulsion Conf. 2008*, Sep. 2008, pp. 1–5.
[24] B. Zhao, Q. Yu, Z. Leng, and X. Chen, "Switched Z-source isolated bidirectional DC/DC converter and its phase-shifting shoot-through bivariate coordinated control strategy," *IEEE Trans. Ind. Electron*., vol. 59, no. 12, pp. 4657–4670, Dec. 2012.
[25] D. Vinnikov, I. Roasto, R. Strzelecki, and M. Adamowicz, "Step-up DC/DC converters with cascaded quasi-Z-source network," *IEEE Trans. Ind. Electron.*, vol. 59, no. 10, pp. 3727–3736, Oct. 2012.
[26] Y. Li, S. Jiang, J. G. Cintron-Rivera, and F. Z. Peng, "Modeling and control of quasi-Z-source inverter for distributed generation applications," *IEEE Trans. Ind. Electron.*, vol. 60, no. 4, pp. 1532–1541, Apr. 2013.
[27] G. A. Covic, J. T. Boys, M. L. G. Kissin, and H. G. Lu, "A three-phase inductive power transfer system for roadway-powered vehicles," *IEEE Trans. Ind. Electron.*, vol. 54, no. 6, pp. 3370–3378, Dec. 2007.
[28] S. Miaosen and F. Z. Peng, "Operation modes and characteristics of the Z-source inverter with small inductance or low power factor," *IEEE Trans. Ind. Electron.*, vol 55, no. 1, pp. 89–96, Jan. 2008.
[29] O. Husev, C. Roncero-Clemente, E. Romero-Cadaval, D. Vinnikov, and S. Stepenko, "Single phase three-level neutral-point-clamped quasi-Z-source inverter," *IET Power Electron.*, vol. 8, no. 1, pp. 1–10, 2015.
[30] I. Roasto, D. Vinnikov, J. Zakis, and O. Husev, "New shoot-through control methods for qi-based DC/DC converters," *IEEE Trans. Ind. Informat.*, vol. 9, no. 2, pp. 640–647, May 2013.
[31] M. Shen, A. Joseph, J. Wang, F. Z. Peng, and D. J. Adams, "Comparison of traditional inverters and Z-source inverter for fuel cell vehicles," in *Proc. Power Electron. Transp.*, Oct. 21–22, 2004, pp. 125–132
[32] N. S. González-Santini, H. Zeng, Y. Yu, and F. Z. Peng, "Z-source resonant converter with power factor correction for wireless power transfer applications," *IEEE Trans. Power Electron.*, vol. 31, no. 11, pp. 7691–7700, Nov. 2016.

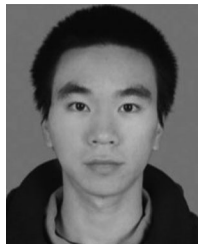

Hulong Zeng (S'12) was born in Guangdong, China, in 1988. He received the B.S. and M.S. degrees in electrical engineering from Zhejiang University, Hangzhou, China, in 2010 and 2013, respectively. He is currently working toward the Ph.D. degree at Michigan State University, East Lansing, MI, USA.

His research interests include power management, ac/dc power converters, and wireless power transfer.

Fang Z. Peng (M'92–SM'96–F'05) received the B.S. degree in electrical engineering from Wuhan University, Wuhan, China, in 1983, and the M.S. and Ph.D. degrees in electrical engineering from the Nagaoka University of Technology, Nagaoka, Japan, in 1987 and 1990, respectively.

From 1990 to 1992, he was a Research Scientist with Toyo Electric Manufacturing Company, Ltd., Toyo, Japan, where he was involved in the research and development of active power filters, flexible ac transmission system (FACTS) applications, and motor drives. From 1992 to 1994, he was with the Tokyo Institute of Technology, Tokyo, Japan, as a Research Assistant Professor, where he initiated a multilevel inverter program for FACTS applications and a speed-sensorless vector control project. From 1994 to 1997, he was a Research Assistant Professor with the University of Tennessee, Knoxville, TN, USA. From 1994 to 2000, he was with the Oak Ridge National Laboratory, where from 1997 to 2000, he was the Lead (Principal) Scientist with the Power Electronics and Electric Machinery Research Center. Since 2000, he has been with Michigan State University, East Lansing, MI, USA, where he is currently a University Distinguished Professor with the Department of Electrical and Computer Engineering. He holds more than 15 patents.

Dr. Peng received many awards including the IEEE/IAS IPCSD 2013 Gerald Kliman Innovator Award, the 2009 Best Paper Award in the IEEE TRANSACTIONS ON POWER ELECTRONICS, the 2011, 2010, 1996, and 1995 Prize Paper Award of Industrial Power Converter Committee in IEEE/IAS; the 1996 Advanced Technology Award of the Inventors Clubs of America, Inc., the International Hall of Fame; the 1991 First Prize Paper Award in the IEEE TRANSACTIONS ON INDUSTRY APPLICATIONS; and the 1990 Best Paper Award in the Transactions of the IEE of Japan, the Promotion Award of Electrical Academy. He was an IEEE TAB Awards and Recognition Committee member and has served the IEEE Power Electronics Society in many capacities: the Chair of Technical Committee for Rectifiers and Inverters, an Associate Editor for the IEEE Power Electronics Transactions, the Region 1.6 Liaison, a Member-atLarge, the Awards Chair, and a Fellow Evaluation Committee member.